Effects of Oxygen Mobility in La-Fe-based Perovskites on the Catalytic Activity and Selectivity of Methane Oxidation

Hui Chang[1], Erlend Bjørgum[2,†], Oana Mihai[2,‡], Jie Yang[1], Hilde Lea Lein[3], Tor Grande[3], Steinar Raaen[4], Yi-An Zhu[1,*], Anders Holmen[2], De Chen[2,*]

[1]United Chemical Reaction Engineering Research Institute (UNILAB), State Key Laboratory of Chemical Engineering, East China University of Science and Technology, Shanghai 200237, China

[2]Department of Chemical Engineering, Norwegian University of Science and Technology, NO-7491, Trondheim, Norway

[3]Department of Materials Science and Engineering, Norwegian University of Science and Technology, N-9491, Trondheim, Norway

[4]Department of Physics, Norwegian University of Science and Technology, N-9491, Trondheim, Norway

KEYWORDS: Perovskite, Surface composition, Methane partial oxidation, Chemical looping.

ABSTRACT: The mechanism and structure requirements of selective and total oxidation of methane in a chemical looping process are both experimentally and theoretically examined on $La_{1-x}Sr_xFeO_{3-\delta}$ (x = 0, 0.2, and 0.5) and $La_{0.5}Sr_{0.5}Fe_{1-x}Co_xO_{3-\delta}$ (x = 0.5 and 1) perovskites. The oxygen mobility in the perovskites described by the formation energy of oxygen vacancy is found to have a pronounced effect on the catalytic activity and selectivity. In particular, the selectivity is controlled largely by the surface oxygen concentration or the oxygen vacancy concentration on perovskites, which depends strongly on the bulk oxygen concentration and the relative rate of the lattice oxygen diffusion with respect to the surface reaction. Substitution of Sr for La at the A site and substitution of Co for Fe at the B site of the ABO_3 perovskites dramatically increase the oxygen mobility. A higher oxygen diffusion rate, and hence enrichment of oxygen on the surface, would improve the catalyst selectivity toward total oxidation.

1. Introduction

The catalytic redox reaction is playing a pivotal role in numerous industrial, environmental, and energy applications, such as selective oxidation for production of fine chemicals in the petrochemical industry[1], total combustion of VOC for environmental protection, and total combustion for energy production[1], oxidative dehydrogenation of alkanes[2], selective catalytic reduction of NO_x[3], electrochemical water splitting, CO_2 reduction[4], and metal air batteries for energy storage[5], etc. Metal oxide catalysts have gained increasing interest to replace noble metal catalysts and gradually become prominent in industrial applications dominated by redox reactions[6]. However, controlling the product selectivity in reactions catalyzed by metal oxides remains a great challenge, which requires fundamental studies to gain a better understanding of the catalytic cycles on the catalyst surfaces. Grasselli[7] proposed the seven-pillar qualitative rule for catalyst design for selective oxidation, where the oxygen mobility that is determined by the M-O bond strength, the concentration of O vacancies, and the nature of O sites is the most important factor controlling the catalytic performance.

There have been increasing efforts to develop the reaction descriptors for rational design of new oxide catalysts or improve industrial catalysts to upgrade the catalytic performance. For example, it has been theoretically and experimentally shown[8] that the apparent activation energy for propene oxidation to acrolein over scheelite-structured, multicomponent, and mixed metal oxides is related to the band gap of the catalyst measured at the reaction temperature. However, a better reaction descriptor is required to bridge the catalyst structure, property, and performance including activity as well as selectivity of the industrial relevant reactions.

Due to the complexity of chemical compositions, structures, and phases of multicomponent metal oxides, it is extremely challenging to develop a viable descriptor on them. The flexibility of the electronic and crystal structure and chemical versatility of ABO_3 perovskites can be used to establish design principles for highly active, selective, and stable catalysts. In addition, owing to their unique

structures and properties[9], perovskite catalysts have been widely applied in the abatement of air pollutants, oxidation reaction, and electrochemical processes for energy storage and conversion[9-13]. In addition, it is widely accepted that most oxidation or oxidative dehydrogenation reactions catalyzed by oxides take place through a Mars van Krevelen mechanism, where lattice oxygen rather than a gas-phase oxidant (e.g., O_2, CO_2, and N_2O) oxidizes the reactant. In most cases, the reoxidation of the surface is fast, and the C-H bond activation in hydrocarbons by surface oxygen leading to the formation of oxygen vacancy is the rate-limiting step[6]. In this sense, methane oxidation on perovskites, where methane is the primary compound of the natural gas and the most stable hydrocarbon molecule with C-H bond, is an attractive model reaction to develop a better relationship between the perovskite properties and catalytic performance such as activity and selectivity.

High temperature (partial) oxidation of methane has been studied on perovskites for synthesis gas production and methane total combustion in both conventional gas-phase reaction and anaerobically in the chemical looping process using lattice oxygen[14-18]. Both the materials and chemistry have been reviewed[6, 10, 19-21]. It has been evidenced that their catalytic activity and property can be significantly influenced by substitution or partial substitution of the A- and/or B-site cations. Co or Mn as the B-site cations in $ABO_{3-\delta}$ perovskites are suggested to be the most promising materials for complete oxidation of hydrocarbons[22-25], while Fe is preferential for selective oxidation[26-27]. The La^{3+} cations are substituted by cations in a lower oxidation state (i.e. Sr^{2+}, Ca^{2+} or Nd^{2+}), leading either to the partial oxidation of the B cations to a higher oxidation state and/or to the formation of oxygen vacancies, which results in a better catalytic activity[22 25].

By virtue of this flexibility, extensive studies have been carried out on perovskites for searching for the parameters determining their catalytic activity[28]. The e_g filling of surface transition-metal cations has been demonstrated as the descriptor of the electrochemical reactions and heterogeneous catalytic reactions[29]. However, the descriptor above was proposed by only considering a single physicochemical property of the transition-metal cations in perovskites for the activity. Because enhancing the catalyst selectivity is still very challenging on mixed transition-metal oxides, The descriptors for selectivity are highly desired for the reactions on perovskites. A large amount of experimental evidence pointed out the importance of the oxygen mobility effects on catalytic performance. However, the oxidation state could change in redox reactions, resulting in the changes in the electronic properties of transition-metal cations and hence in the change of the oxygen mobility, which makes it challenging to predict the dependence of the activity and selectivity on the properties of perovskites[30].

In a previous study, we have demonstrated that the oxygen mobility effects on activity and selectivity in methane oxidation could be tuned by the crystal size of the perovskite $LaFeO_3$[27]. In the present work, we will investigate the effects of substituting Sr^{2+} for La^{3+} in $LaFeO_{3-\delta}$ and the substitution of Co^{3+} for Fe^{3+} in $La_{0.5}Sr_{0.5}FeO_{3-\delta}$ on the oxygen mobility and the activity and selectivity of methane oxidation. Through substitution of the lower valence Sr^{2+} ion for La^{3+}, the amount of oxygen vacancy defects and the oxidation state of Fe can be tuned. Substitution of Co^{3+} for Fe^{3+} can significantly alter the transition-metal cation properties and oxygen mobility.

The present study is focused on experimentally and theoretically searching for the correlations among the perovskite composition, properties, and catalytic performance in methane oxidation. The oxygen mobility is studied by first-principles calculations theoretically, and the catalytic performance of perovskites in methane oxidation is examined by temperature programed reduction (TPD), temperature programed surface reactions (TPSR), UV-Vis absorption spectra, and the X-ray photoelectron spectroscopy (XPS) experimentally. The results bridge the C-H activation activity and selectivity with the oxygen mobility of perovskites described by oxygen diffusivity and oxygen vacancy formation energy.

2. Experimental and computational details

2.1. Catalyst preparation

$La_{1-x}Sr_xFeO_{3-\delta}$ (x = 0, 0.2) perovskites were synthesized by the glycine-nitrate combustion method[31]. Aqueous solutions of stoichiometric nitrates amounts (Acros, Merch or Fluka, p.a.) were made, and glycine (Merch, p.a.) was added as a complexing agent in a glycine/nitrate mole ratio of 5/9. The water content in the nitrates was determined by thermogravimetric analysis by heating the nitrates to 1273 K for 24 h and weighing the resulting oxides to determine the exact amount of cations in the nitrate salts. The solutions were evaporated in a glass tube while heated until the resulting gel ignited for decomposition to oxide. The oxides were pre-calcined by allowing them to fall through a vertical alumina tube preheated to 1073 K ~ 1173 K. The resulting oxide powders were ball-milled (Si_3N_4-balls) overnight in 100% ethanol. The milled powders were further calcined at 900 °C for 10 h in air.

$La_{0.5}Sr_{0.5}Fe_{1-x}Co_xO_{3-\delta}$ (x = 0, 0.5, and 1) were synthesized by spray drying method. The aqueous glycine/nitrate solutions were dried in a Büchi Mini Spray Dryer B-191 with hot air (150 °C) as the drying medium. The resulting solid precursors were ignited for decomposition to oxide by allowing it to fall through a vertical alumina tube preheated to 1073 K ~ 1173 K. The resulting oxide powders were ball-milled (Si_3N_4-balls) overnight in 100% ethanol or iso-propanol. The milled powders containing Co (x = 0.5 and 1) were further calcined at 900 °C for 24 h in air while the Fe containing powders (x = 0) were calcined at 1173 K for 10 h in air.

2.2. Characterization

X-ray diffraction studies were performed in a Siemens D5005 powder X-ray diffractometer using Cu Kα radiation and a secondary monochromator. XRD patterns were collected in the range of 2θ from 20 ° to 70 ° for all the samples. BET measurements were performed by using a Micrometrics TriStar 3000 instrument. The samples were outgassed overnight under vacuum at 473 K before

measurement. The temperature-programmed reduction (TPR) was carried out in a U-shaped tubular quartz reactor. The amount of 0.2 g catalyst was loaded and heated at a rate of 10 K/min to 1173 K with a gas consisting of 7% H_2 in Ar. The gas flow was 50 ml/min. Temperature programmed surface reaction (TPSR) was conducted in a conventional quartz fixed-bed reactor and the amount of 0.25 g catalyst was employed. Before the TPSR experiments, the sample was heated from room temperature to 1173 K at a rate of 15 K/min under a gas mixture of O_2 and Ar and then held at this temperature for 10 minutes. Compared to TPR, the heating rate was increased to 15 K/min and the weight of catalyst was increased to 0.25 g to get stronger MS signals during heating. Subsequently, the catalyst was cooled down to 373 K under the same atmosphere followed by heating up to 1173 K at a rate of 15 K/min with 7 ml/min CH_4 and 33 ml/min Ar. The total gas flow rate was 40 ml/min.

The adsorption edge energies of perovskites were obtained from diffuse reflectance UV-Vis absorption spectra using a Shimadzu (UV-2401PC) spectrophotometer with an ISR-240A integrating sphere assembly. The $BaSO_4$ standard whiteboard was used as a reference. The samples were diluted with $BaSO_4$ (ratio 1:5) and mixed. The adsorption edge energy was estimated from the x-intercept of a linear fit to the adsorption edge. The Kubelka-Munk function for infinitely thick samples $F(R_\infty)$[32] was used to convert diffuse reflectance data into absorption spectra.

The X-ray photoelectron spectroscopy (XPS) analysis was performed in a hemispherical SCIENTA SES 2002 electron energy analyser using a monochromatized Al Kα X-ray source (GammaData Scienta) with a total energy resolution of about 0.4 eV. All spectra were measured in an angle integrated mode around normal emission. The surface compositions in mole % were estimated by the measured areas of the element peaks divided by the corresponding atomic sensitivity factors, which were determined by a Matlab program applying a Shirley background.

2.3. Kinetic study

The experiments were carried out using a quartz fixed-bed reactor. The amount of 1 g catalyst was fixed on a quartz sinter and a vertical electrical furnace was used for heating. The product composition was followed by an on-line GASLAB 300 mass spectrometer. In order to simulate the chemical looping process for methane conversion, switches between flows of O_2/Ar and CH_4/Ar were performed. The perovskites were oxidized by 10 ml/min O_2 in Ar and then reduced by 7.2 ml CH_4 in Ar. Between the switches, the reactor system was flushed with Ar to avoid mixing CH_4 and O_2. Throughout the experiments the total flow rate was kept at 40 ml/min. For oxidation, 10 ml/min O_2 in Ar was used, while the CH_4 flow rate varied from 2.5 to 16 ml/min CH_4 in Ar. Most experiments were performed at 1173 K.

2.4. DFT calculation

All plane wave DFT calculations were carried out using the VASP code[33-34]. The projector-augmented wave (PAW) method[35] and the BEEF-vdW functional[36] were used to provide a accurate description of the bonding in the bulk and on the surface of perovskites. For the "hard" PAW potentials, a plane wave energy cutoff of up to 600 eV was found to be necessary to converge the total energy per atom to within 1 meV. Sampling of the Brillouin zone was performed with the Monkhorst-Pack method[37] and electronic occupancies were determined by the Gaussian smearing method with an energy smearing of 0.1 eV. Because the standard exchange-correlation functionals suffer from excessive electron delocalization[38], an additional Hubbard-type term was applied by introducing an effective interaction parameter U_{eff}. The used U_{eff}

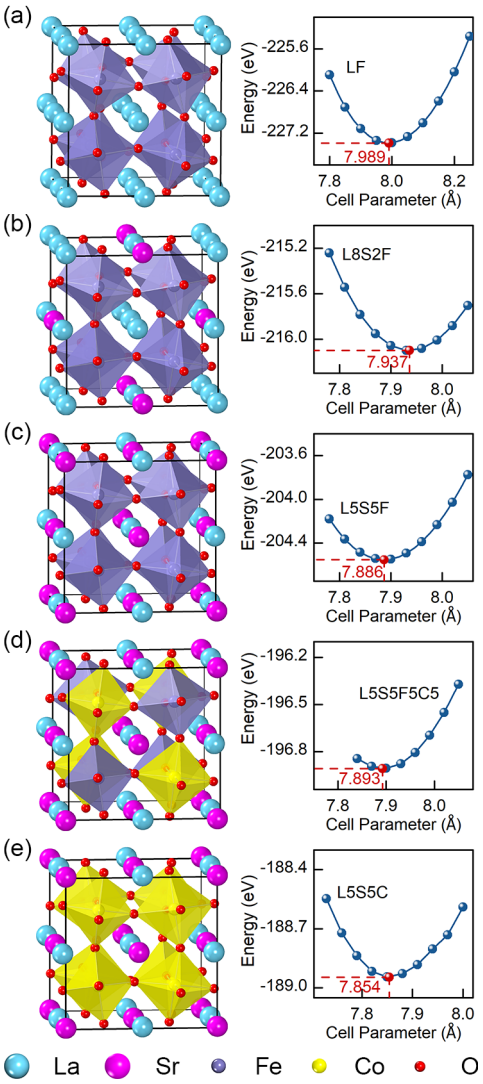

Figure 1. Schematic representations of the bulk structures of (a) $LaFeO_3$ (LF), (b) $La_{0.8}Sr_{0.2}FeO_3$ (L8S2F), (c) $La_{0.5}Sr_{0.5}FeO_3$ (L5S5F), (d) $La_{0.5}Sr_{0.5}Fe_{0.5}Co_{0.5}O_3$ (L5S5F5C5), and (e) $La_{0.5}Sr_{0.5}CoO_3$ (L5S5C).

values for Fe and Co are 2.9 and 3.1[39], respectively, which prove to be able to predict with reasonable accuracy the physical and chemical properties of the $LaFeO_3$ and $LaCoO_3$ perovskites, such as band gap, magnetic moment, and oxygen vacancy formation energy[39]. For the magnetic substances, spin-polarized calculations were carried out

self-consistently to obtain reasonably accurate structures and energetics.

It was found that at high reaction temperatures (700 K ~ 1200 K) the crystal structure of the perovskites adopts a pseudocubic symmetry[40]. Hence, a 2 × 2 × 2 replication of the ideal cubic unit cell was first constructed for $LaFeO_3$ (denoted as LF). Then, the pseudocubic structures were obtained by imposing an $a^-b^+a^-$ tilt system[41] and allowing for internal atomic relaxation. As for the doped and substituted perovskites, the La^{3+} and/or Fe^{3+} cations were partially or completely replaced with Sr^{2+} and/or Co^{3+} cations, giving rise to $La_{0.8}Sr_{0.2}FeO_3$ (denoted as L8S2F), $La_{0.5}Sr_{0.5}FeO_3$ (L5S5F), $La_{0.5}Sr_{0.5}Fe_{0.5}Co_{0.5}O_3$ (L5S5F5C5), and $La_{0.5}Sr_{0.5}CoO_3$ (L5S5C), as shown schematically in Figure 1. The lattice constants of the pseudocubic supercells were obtained by first performing a series of constant-volume calculations and then fitting the energy vs. volume data to the Murnaghan equation of state[42]. The calculated cell parameters were applied in subsequent calculations of oxygen vacancy formation energies and migration barriers. A 3 × 3 × 3 k-point grid was used to sample the first Brilloiun zone of the structural models. Atomic charges were calculated through the Bader charge analysis. The dimer method was used to locate the transition states for oxygen migration in bulk perovskite. When the forces on each atom were less than 0.03 eV/Å, both the geometry optimization and transition state search were considered to be converged.

3. Results and discussion

3.1 Tolerance factor, XRD characterization, and BET surface area

Perovskite oxides have the general formula ABO_3 where the 12-coordinated A sites may be occupied by large ions with r_A > 0.90 Å and the 6-coordinated B sites are usually occupied by transition-metal cations with r_B > 0.51 Å[23, 43]. The high stability of the perovskite structure allows the partial substitution of either A or B site cations by other metals with different oxidation states and consequent creation of structural defects such as anionic or cationic vacancies[23,44]. A useful crystal-chemistry tool for the perovskite structure is the tolerance factor *t*. The *t* value of perovskites must be in the range of 0.80 ~ 1.0[45-46] and can be expressed by:

$$t = \frac{r_A + r_O}{\sqrt{2}\cdot(r_B + r_O)} \quad (1)$$

where r_A, r_B, and r_O are the ionic radius of the A, B, and oxygen ion, respectively. The tolerance factor shows how far ideal packing the ionic sizes can move from and still be "tolerated" by the perovskite structure and it reflects the structural distortion of the perovskite[46]. Table 1 shows that the obtained values of the tolerance factors are in the range of 0.8 ~ 1.0 for all the compositions of interest, which indicates a cubic symmetry or symmetry close to cubic, e.g., orthorhombic and rhombohedral. In the calculations of tolerance factors, Fe is assumed to have a high oxidation state of +3 and the formal oxidation state of +3 is assigned to Co as well. By replacing La^{3+} with a larger-radius ion such as Sr^{2+}, the tolerance factor increases, which indicates an increased symmetry in the materials.

Table 1. Tolerance factor, average crystallite thickness, and BET surface area of produced perovskites

Perovskite	Tolerance factor	Average crystallite thickness, nm	BET surface area, m^2/g_{cat}
LF	0.842	29	3.2
L8S2F	0.853	20	4.6
L5S5F	0.868	23	4.9
L5S5F5C5	0.875	13	5.4
L5S5C	0.881	17	5.1

The XRD patterns for the prepared perovskites are shown in Figure 2a. From the figure, it is clear that all the materials are considered as orthorhombic perovskite structures, with the (121) reflection being the most intense diffraction peak. As indicated by the shift to higher 2θ degree, the Sr-substitution and Co-containing perovskites result in a smaller pseudocubic unit cell of the materials[47]. These observations can be rationalized by the ionic radii of the cations[48]. The estimated average crystallite size based on the Scherrer equation and the BET specific surface area of the pervoskites are also listed in Table 1, which are found to decrease and increase, respectively, upon substitution of Sr^{2+} and Co^{3+} for La^{3+} and Fe^{3+}.

3.2 TPR results

The TPR results of the five perovskites are shown in Figure 2b and Table 2. The hydrogen consumption is close to zero for LF in the temperature range of 373 K ~ 1173 K and only a small hydrogen uptake occurs from 1073 K as

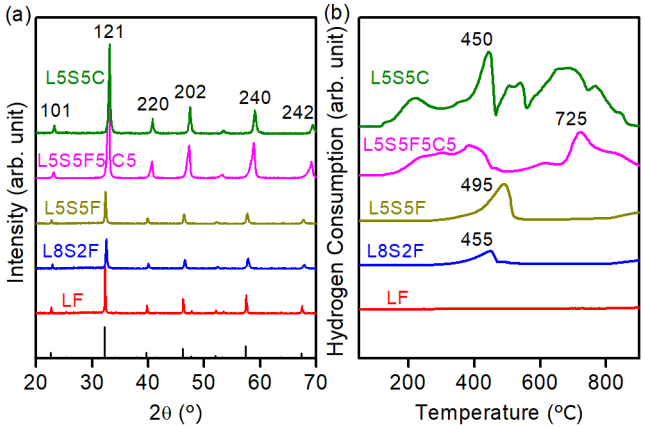

Figure 2. (a) X-ray diffraction (XRD) spectra and (b) TPR profiles of different perovskites prepared.

L5S5F has a larger peak compared to L8S2F, demonstrating that the amount of reducible oxygen released during reaction increases with the Sr^{2+} content in the materials[49], as shown in Figure 2b. Several peaks are observed for both the L5S5C and L5S5F5C5 perovskites, which indicates many different sites or mechanisms for releasing oxygen during TPR. Partial substitution of Sr^{2+} for La^{3+} in La_{1-}

$_xSr_xFeO_{3-\delta}$ requires charge compensation which is achieved either by the formation of anion vacancies:

$$La^{3+}Fe^{3+}O_3 + x \cdot Sr_x^{2+} - x \cdot La^{3+} - \frac{x}{4}O_2 = La_{1-x}^{3+}Sr_x^{2+}Fe^{3+}O_{3-(x/2)} \quad (2)$$

or by the increase in the average oxidation state of Fe from Fe^{3+} to Fe^{4+} (eq. 3)[22 25]:

$$La^{3+}Fe^{3+}O_3 + x \cdot Sr_x^{2+} - x \cdot La^{3+} = La_{1-x}^{3+}Sr_x^{2+}Fe_{1-x}^{3+}Fe_x^{4+}O_3 \quad (3)$$

The combination of (eq. 2) and (eq. 3) can be described as

$$La^{3+}Fe^{3+}O_3 + x \cdot Sr_x^{2+} - x \cdot La^{3+} - \frac{x-z}{4}O_2 = La_{1-x}^{3+}Sr_x^{2+}Fe_{1-z}^{3+}Fe_z^{4+}O_{3-(x/2)+(z/2)} \quad (4)$$

Thus, the substitution of Sr^{2+} for La^{3+} in A site of ABO_3 structure results in the formation of Fe^{4+} and/or oxygen vacancies. The increased hydrogen consumption upon substitution of Sr^{2+} for La^{3+} was also observed by Li et al.[43]. Due to the relatively easy redox process between Fe^{4+} and Fe^{3+}, larger quantities of oxygen are available at low temperature in the materials, which may be ascribed to faster oxygen diffusion rate in the bulk with higher Sr-substitution, and the overall oxidation activity is enhanced[50].

The results in Figure 2b and Table 2 indicate that the B-site substitution of Fe by Co in ABO_3 significantly increases the release of oxygen from the material, suggesting an enhanced oxygen mobility. In addition, the H_2 consumption that is larger for L5S5C than for L5S5F5C5 reveals that a large degree of Fe substitution by Co results in a higher oxygen mobility. It is consistent with reported observation that the lattice oxygen is desorbing above 300 °C during oxygen temperature programmed desorption from $La_{1-x}Sr_xCoO_{3-\delta}$ ($x > 0$)[51]. According to Zhang et al.[25], the charge compensation when replacing La^{3+} with Sr^{2+} induces more oxygen vacancies in $La_{1-x}Sr_xCoO_{3-\delta}$ perovskites than in $La_{1-x}Sr_xFeO_{3-\delta}$. The difference in oxygen release between the Fe and Co containing perovskites can therefore be explained by the difference in the stability of the Fe^{4+} and Co^{4+} ions. The Co-containing perovskites will have a higher tendency to release oxygen by the reduction of Co^{4+} to Co^{3+} which is a more stable oxidation state[52]. The presence of Fe together with Co in the B site of the perovskite structure is likely to stabilize a high oxidation state, as compared to only Co in the B site[25]. Because Fe^{4+} is more stable than Co^{4+}, the stabilization is caused by a reduced number of oxygen vacancies when Fe is introduced into the structure.

Table 2. Hydrogen consumption during the temperature-programmed reduction (TPR) of perovskites. Heating rate: 10 K/min to 1173 K, P_{H_2} = 0.14 bar, P_{Ar} = 0.84 bar, WHSV = 1680 ml H_2/(hr.g).

Perovskite	H_2 consumption, μmol/g_{cat}
LF	80
L8S2F	320
L5S5F	880
L5S5F5C5	2400
L5S5C	5900

3.3 TPSR characterization

The TPR results reveal a very low reducibility in hydrogen stream for the Fe-based perovskites (LF, L8S2F, and L5S5F). The reducibility of these perovskites is tested in methane instead of hydrogen by TPSR. The surface reaction between methane and the perovskites is examined while linearly increasing the temperature. As is shown in Figure 3, there are two major periods for methane consumption during TPSR. First is a methane consumption at around 350 ~ 550 °C and secondly methane is consumed from 600 ~ 700 °C up to 900 °C. The amount of methane consumed and the starting point for the reaction vary for all three perovskites.

The first peak at around 350 ~ 550 °C is only present for the Sr-based perovskites. Both L8S2F (Figure 3b) and L5S5F (Figure 3c) have peaks showing methane consumption with a maximum around 500 °C, but for

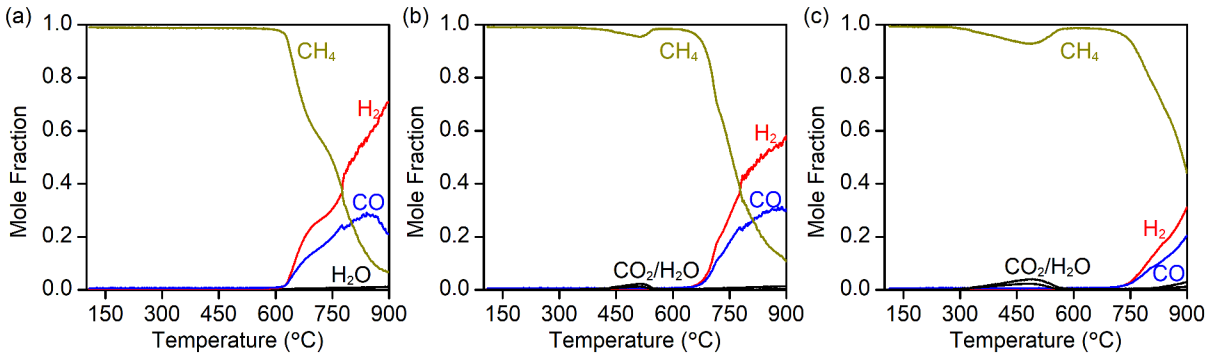

Figure 3. TPSR profiles for the reactions between methane and (a) LF, (b) L8S2F, and (c) L5S5F. Heating rate: 15 K/min to 1173 K, P_{CH_4} = 0.14 bar, P_{Ar} = 0.84 bar, WHSV = 1680 mlCH4/(hr.g). The mole fraction is normalized in the absence of inert gas.

L5S5F this peak is larger and wider. In both the cases the reacting methane produces only CO_2 and water. Seiyama[22] found that the substitution of Sr^{2+} in $La_{1-x}Sr_xCoO_{3-\delta}$ perovskites produces oxygen vacancies using temperature-programmed desorption of oxygen. The oxygen desorbing at low temperatures is related to the removal of weakly bonded oxygen on or close to the surface[22]. The TPSR results indicate that this surface oxygen contributes to total oxidation of hydrocarbons.

The amount of CO_2 and H_2O generated by the total oxidation follows the order L5S5F > L8S2F > LF. These results suggest that the substitution of La by Sr in the A site enhances the oxygen mobility and the higher degree of substitution would enhance the mobility of oxygen to a greater extent.

The second area of methane consumption in Figure 3 starts roughly at 600 °C for LF, around 650 °C for L8S2F, and about 700 °C for L5S5F to form the synthesis gas as a result of the partial oxidation. The amount of water and CO_2 produced as products of total combustion is relatively low at high temperatures for all the three perovskites. The ordering of the onset temperature of the second peak is opposite to the expectation, where the onset temperature is expected to be lower for the perovskites with higher oxygen mobility. Hence, the onset temperature depends possibly not only on the mobility of the oxygen but also on the surface oxygen concentration. Owing to a high energy barrier[53], oxygen diffusion is slower at relatively low temperatures, and the surface oxygen concentration is lower on the perovskites where more oxygen is consumed at low temperatures. When the reaction temperature is approaching 900 °C over LF, the H_2 concentration increases while the CO decreases, which can be attributed to the methane decomposition and coke formation during the reaction.

Comparison between TPSR and TPR clearly points out that the methane is a stronger reductant than hydrogen for the Fe-based perovskites. The significant difference is consistent with the reported observation[54]. No activity of hydrogen on LF was observed, while a large amount of oxygen was removed when methane is introduced. It suggests that the selectivity toward synthesis gas could be higher on the Fe-containing perovskites.

3.4 Kinetic study of methane oxidation over different perovskites

The partial oxidation of methane to synthesis gas was performed by using the lattice oxygen of different perovskite oxides as oxygen source at 1173 K for 6 minutes. The time on stream (TOS) of 6 minutes was optimized in our preliminary experiments, where the oxygen is only partially removed. A too long TOS will result in a significant carbon formation, especially on the LF catalyst. Figure 4 shows the transient responses after switching the WHSV from 40 ml/min Ar to 7.2 ml CH_4/33 ml/min Ar for the five catalysts. Two separate reaction periods are observed in all the experiments. Initially, the reaction is very fast and CH_4 is fully combusted into water and CO_2, which is a total oxidation region. When the oxygen species in the surface are gradually consumed, the amount of CO_2 and water decreases and CO and H_2 start to be produced which is a partial oxidation region. The rates of CO and CO_2 formation as a function of

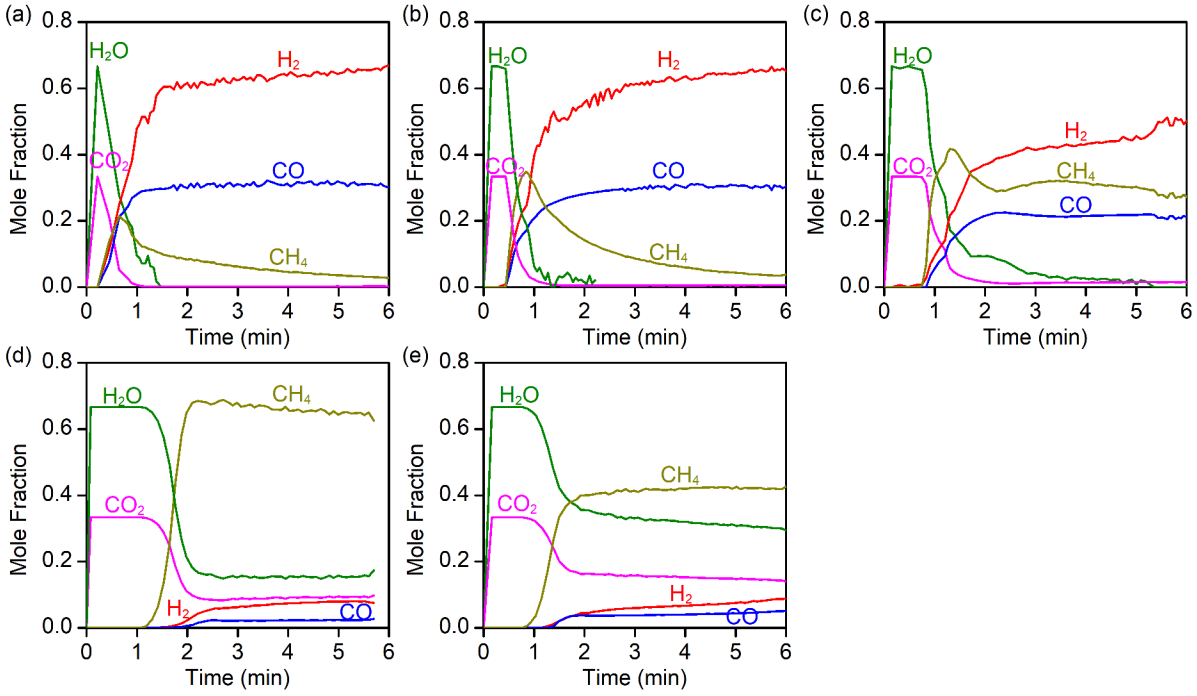

Figure 4. Results from reaction of CH_4 with various perovskites at 1173 K presented by mole fractions of the gases as a function of reduction time: (a) LF, (b) L8S2F, (c) L5S5F, (d) L5S5F5C5, and (e) L5S5C. Reaction conditions: $T_{furnace}$ = 1173 K, 1g catalyst, P = 1 atm, P_{CH_4} = 0.18 atm, WHSV = 432 $mLCH_4/(hr{\cdot}g_{cat})$.

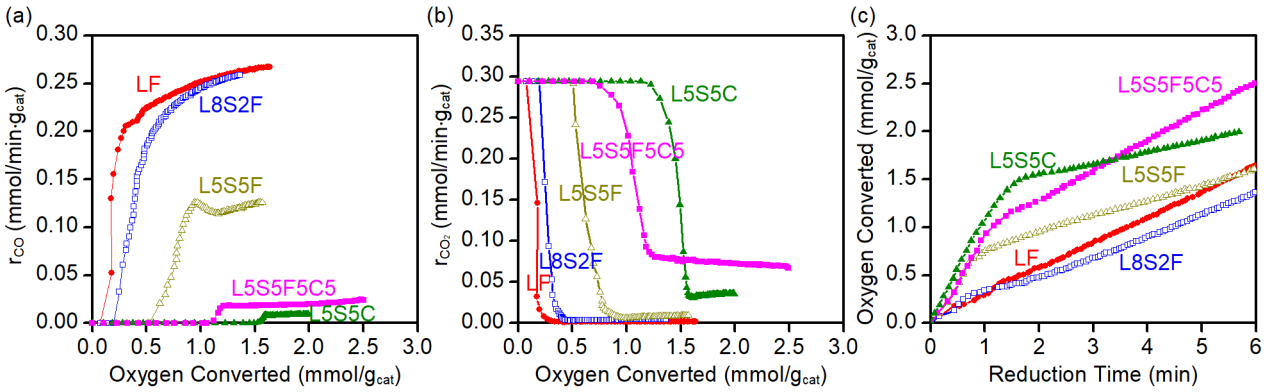

Figure 5. Catalytic oxidation of methane over different perovskites during 6 minutes reduction: the site yield of (a) CO and (b) CO_2 as a function of the total amount of oxygen converted and (c) the total amount of oxygen converted during 6 minutes reduction over various perovskites. Reaction conditions: T = 1173 K, 1g catalyst, P = 1 atm, WHSV = 432 mLCH_4/hr·g_{cat}, reaction time: 6 min.

oxygen (O) removed (mmol/g_{cat}) are shown in Figure 5a and Figure 5b, respectively. Figure 5 reveals that the first part of oxygen in perovskites is selectively converted to CO_2 by the total oxidation of methane. The amount of oxygen contributed to the total oxidation depends significantly on the catalyst composition.

For the $La_{1-x}Sr_xFeO_{3-\delta}$ perovskites (see Figure 4a, Figure 4b, and Figure 4c), methane was consumed completely at the initial total oxidation period, and then goes through a maximum following a rapidly decrease with TOS. The conversion of methane is almost 100% for all the catalysts studied here. It is clearly indicated that the rate of the total combustion is larger than that of the partial oxidation. There is a threshold of oxygen amount removed from the $La_{1-x}Sr_xFeO_{3-\delta}$ perovskites (see Figure 5b), after that there is almost no formation of CO_2. In the region of the partial oxidation (see Figure 4 a-c), a relatively stable formation of CO and H_2 was observed, producing H_2 and CO with a ratio close to 2:1. The threshold of oxygen amount follows the order LF < L8S5 < L5S5 (see Figure 5b). The partial substitution of La^{3+} by Sr^{2+} leads to a larger amount of oxygen converted to CO_2 and H_2O. The higher degree of substitution of Sr increases the amount of the total oxidation products to a greater extent. However, the total methane conversion decreases by increasing the Sr^{2+} content in the perovskites.

For the Co containing perovskites where the B site in the $La_{0.5}Sr_{0.5}FeO_{3-\delta}$ is substituted by Co with different degrees, the amount of oxygen leading to the total oxidation is found to be much larger than Fe-based perovskites. Methane was also completely converted in the total oxidation region on L5S5F5C5 and L5S5C in Figure 4d and Figure 4e, respectively. After the oxygen threshold, the partial oxidation to CO and H_2 occurs where methane conversion is relatively low and also a significant amount of the total oxidation products is observed. The average CO selectivity upon 6 minutes reduction shown in Table 3 follows the order LF > A-site-substituted perovskites (L8S2F, L5S5F) > B-site-substituted perovskite (L5S5F5C5) > Co-based perovskite (L5S5C). The Co-substituted perovskites seem to be promising as catalysts for the total methane oxidation instead of the partial oxidation. The results clearly illustrate the flexibility of the properties of ABO_3 perovskites, and methane oxidation can be tuned to form nearly pure partial oxidation or pure total oxidation.

Figure 5c depicts the variation of the amount of O removed from the materials with TOS in the reduction step. The slope of the oxygen converted vs. the reduction time plot at the initial period represents the initial reaction rate. It can be seen from the figure that the amount of O removed with 6 minutes follows the order L5S5F5C5 > L5S5C > L5S5F > LF > L8S2F. It should be noted that not all the oxygen is removed during the 6 minutes reduction. For the LF, the maximum amount of the removable oxygen is about 3.5 mmol/g, which is related to Fe^{3+} reduced to Fe^{2+} [26-27]. The effects of substitution of A and B sites are more significantly on the selectivity compared to the conversion. Figure 5b reveals that the first part of oxygen is very active for the total combustion of methane. The amount of these active oxygen increases with the amount of the A-site substitution (Sr^{2+} for La^{3+}) and more significantly with the B-site substitution (Co^{3+} for Fe^{3+}), which may be attributed to the more rapid replenishment of lattice oxygen leading to high concentration of surface oxygen, which will be discussed later. It should be noted that the order of oxygen removal rate is opposite to the order of the total amount of methane converted for 6 minutes reduction shown in Table 3, where A-site and B-site substitution in ABO_3 (LF) lower the methane conversion. The difference in the order of O removal and methane conversion is related to the selectivity and the stoichiometry of the reaction, and one mole of CO_2 formation requires two oxygen atoms, while one mole of CO formation requires only one oxygen atom.

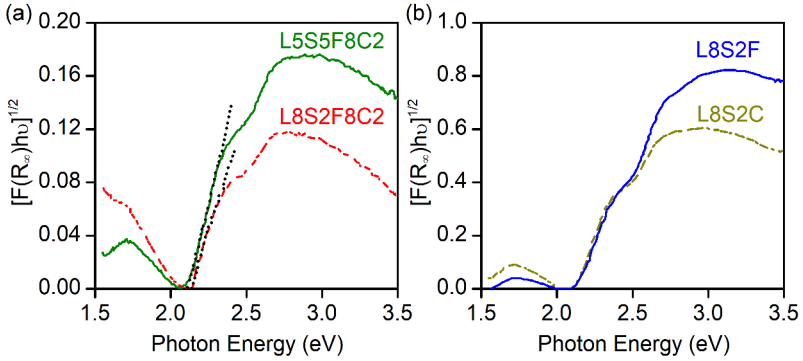

Figure 6. Diffuse reflectance UV-vis absorption spectra of various perovskites. Comparison (a) between $La_{0.5}Sr_{0.5}Fe_{0.8}Co_{0.2}O_{3-\delta}$ (L5S5F8C2) and $La_{0.8}Sr_{0.2}Fe_{0.8}Co_{0.2}O_{3-\delta}$ (L8S2F8C2) and (b) between L8S2F and $La_{0.8}Sr_{0.2}CoO_{3-\delta}$ (L8S2C).

Table 3. Total methane conversion and CO selectivity during 6 minutes reduction at 1173 K for different perovskites

Perovskite	CH_4 conversion (%)	CO selectivity (%)
LF	82	92
L8S2F	75	82
L5S5F	49	65
L5S5F5C5	39	15
L5S5C	27	9

By increasing the Sr^{2+} content, the amount of removable O from the perovskites will increase and a larger amount of CO_2 is formed. Both Fe and Co in the B site of perovskites seem to stabilize a high oxidation state compared to only Co in the B site, as shown by Zhang et al.[25] and a larger amount of CO_2 is presented than by the samples without the Co^{3+} content. Both the increasing Sr^{2+} content and the B-site substitution (Co^{3+} for Fe^{3+}) result in more removable O from the catalysts. Considering the selective oxidation, the difference between the Co and non-Co-based-Fe perovskites can be explained. The Co-O bonds are weaker than Fe-O bonds, resulting in higher ion mobility and faster oxygen diffusion in the bulk, which favors the total combustion products[55]. During methane partial oxidation experiments, no carbon was observed during regeneration except for the LF perovskite. The carbon formation during the reduction step was therefore removed as CO during re-oxidation of catalysts. However, no carbon was observed after five reduction-oxidation cycles, during which the H_2/CO ratio slightly above 2 is produced (see Figure S1 in the Supporting Information). The methane conversion was around 70% with high selectivity toward CO of around 98%.

The change in the surface composition of the mixed oxides gives rise to changes in the electronic properties of these materials[56]. Figure 6a shows that the absorption edge energy slightly shifts to higher energy when La^{3+} and Sr^{2+} have different contents in the perovskite structure. By replacing Fe^{3+} with Co^{3+}, no significant changes in the absorption edge energy are made, as shown in Figure 6b.

3.5 XPS results

Co2p XPS spectra for three samples are presented in Figure 7a. The $2p_{1/2}$ component has been deconvoluted into two components for the top and bottom spectra. The high binding energy component most likely corresponds to the Co^{3+} oxidation state whereas the low binding energy component most likely corresponds to the Co^{2+} oxidation state. As for the Co^{2+}, roughly 80% of the spectral weight is indicated for $La_{0.8}Sr_{0.2}Fe_{0.8}Co_{0.2}O_3$ (L8S2F8C2) and about 74% for $La_{0.8}Sr_{0.2}CoO_3$ (L8S2C). The XPS spectrum of $La_{0.5}Sr_{0.5}Fe_{0.8}Co_{0.2}O_3$ (L5S5F8C2) has not been curve fitted. However, in this case, cobalt seems to be predominantly in the +2 oxidation state. It should be mentioned that the wide structure between the two Co2p components in the XPS spectra corresponds to a Fe Auger transition which makes a complicated deconvolution of the $Co_{3/2}$ components.

Figure 7b shows the $Fe2p_{3/2}$ XPS spectra of the L8S2F8C2, L5S5F8C2, and L8S2F perovskites. These spectra have been deconvoluted into three peaks (a, b, and c), as indicated in Figure 7b, which is the smallest number of peaks that are required to obtain a reasonably good fit to the data. However, peak fitting of wide structures shown in the present XPS is complicated and the given fits are only examples how it may be done using three peaks. Peak positions depend on the oxidation state as well as local coordination of the Fe atoms in the given samples, and the number of unresolved components to the peaks cannot be determined. Peak (a) would be consistent with Fe^{2+} in FeO while peak (b) may correspond to Fe^{3+} in Fe_2O_3. Peak (c) at the binding energy above 713 eV can be ascribed to Fe^{3+} in the tetrahedral position[57] and also possibly to Fe^{4+} [58] With respect to the intensity of each peak in the XPS spectra, the domination of the peaks (a) and (b) follows values from top to bottom: 48%, 47%, 40%, and 29%, 32%, 37%, respectively.

The O1s XPS spectra for the prepared perovskites are shown in Figure 7c, which have been deconvoluted into four peaks A ~ D. The lowest number of peaks in the deconvolution giving a fairly good fit to the data is found to be four. Considering the XPS interpretation[59], the lowest binding energy peak may be assigned to lattice O

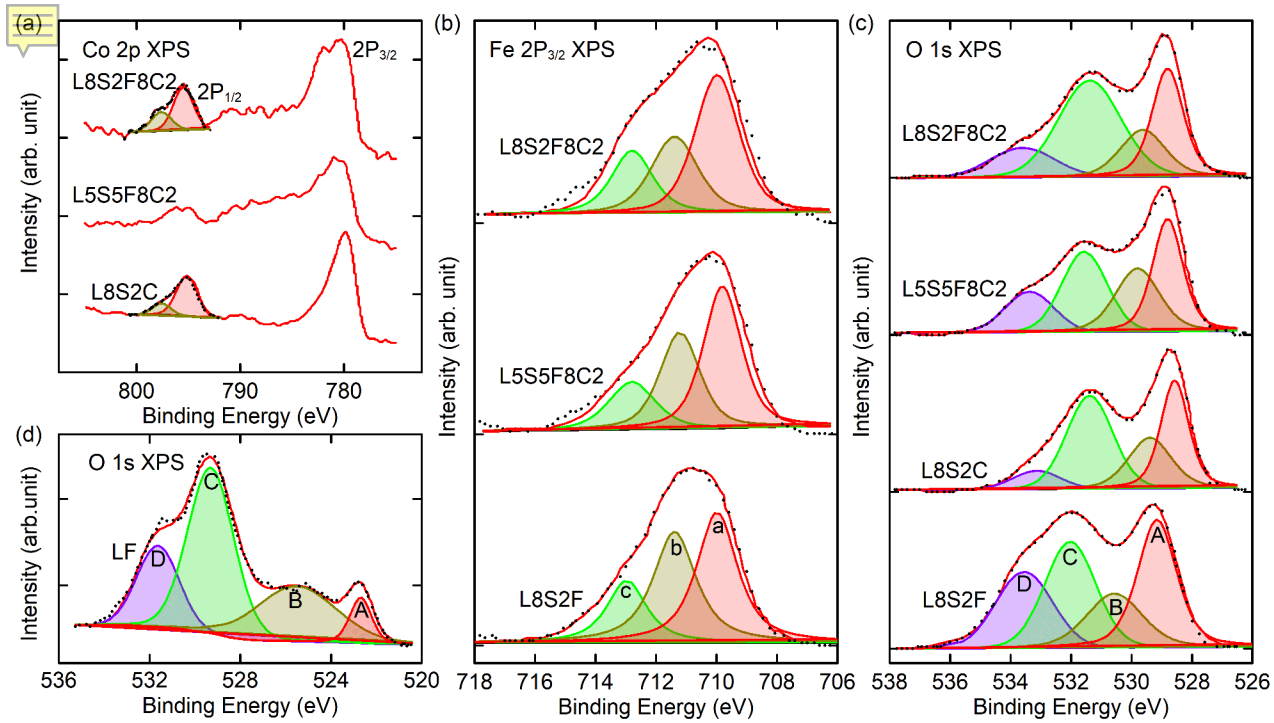

Figure 7. (a) Co2p, (b) Fe2p$_{3/2}$, and (c) O1s XPS spectra of fresh L8S2F8C2, L5S5F8C2, L8S2C, and L8S2F perovskites. (d) O1s XPS spectra of fresh LF perovskite Deconvolution analysis of Fe2p$_{3/2}$ and O1s signals. The dotted line corresponds to the raw data, and the thin solid line refers to the spectra envelope. The thin solid lines under the main dotted line refer to the spectral components named as a ~c and A ~ D peaks

species. Peak B can be associated with Fe/Co/Sr-oxide while the peaks C and D can be assigned to chemisorbed surface O or hydroxides species. In particular, the peaks D can be attributed to the adsorbed water species. The peaks C and D are assigned based on the observation that the rare earth oxides tend to be hygroscopic when exposed to atmospheric conditions[59-60].

The O1s XPS spectra for the LF perovskite are shown in Figure 7d. Two species of oxygen are shown in the O1s XPS spectra. The chemisorbed O or OH^- species correspond to the binding energy between 530 and 534 eV while the lattice oxygen species correspond to the binding energy between 527 and 531 eV[58, 61]. The other two peaks in the binding energy range of 521 to 528 eV can be attributed to the adsorbed water species or mixed oxides. The relative intensities and the maximum values of binding energies of O1s XPS peaks for various perovskite samples are summarized in Table 4.

3.6 Tuning the selectivity of methane oxidation by manipulating the ABO_3 perovskites

Perovskites ABO_3 have been widely applied into heterogeneous reactions such as combustion and partial oxidation, which can serve as a platform for rational catalyst design. Although the present work focuses on the chemical looping of methane reforming process, combing reduction and oxidation steps together represent the catalytic cycle of the heterogeneous total or partial oxidation of metal on perovskite surfaces. Here we attempt to provide a general principle both from experimental results and theoretical calculations for tuning catalyst activity and selectivity by means of selective substitution in ABO_3.

The TPR experiment indicates that the LF perovskite is very stable (see Figure 2b), where La and Fe are all trivalent and the B-site cation is approximately single Fe^{3+} and in a stable state with the 3d orbitals half-filled ($t_{2g}^3e_g^2$)[58]. The XPS study suggests that part of Fe is quadrivalent (+4) when the A sites (La^{3+}) are partially substituted by Sr^{2+}. The unfilled Fe 3d orbitals have an unstable state, and Fe^{4+} can easily lose the electron on the e_g band to be Fe^{5+} or get another electron to be half-filled during reduction process. Meanwhile, it generates oxygen vacancy sites in the perovskite structure to maintain the neutrality[58]. The XPS results are consistent with the observation of TPR. The substitution of Sr^{2+} for La^{3+} increases the concentration of Fe^{4+}, and thus the reduction ability is enhanced with the increasing Sr^{2+} amount (see Figure 2b). Meanwhile, the increasing Sr^{2+} amount gives rise to more oxygen vacancies, thus increasing the adsorbed oxygen amount, as indicated in Table 4.

From the viewpoint of chemical bonding, the electronegativity of the B ion is higher than that of La, which leads to localization of the electrons on the 3d orbitals in the compound and, consequently, to the increase in the electron density around B and O. The stronger electronegativity of Co than Fe causes the enhanced ability of electron transfer between HOMO and

Table 4. The relative intensities and maximum binding energy of the A ~ D peaks for O1s XPS spectra

Perovskite	Peak intensity (%)				Maximum binding energy (eV)			
	A	B	C	D	A	B	C	D
L8S2F	31	14	31	24	529.2	530.7	532	533.6
L8S2C	29	18	44	9	528.5	529.5	531.4	533.2
L5S5F8C2	29	24	32	15	528.8	529.9	531.7	533.4
L8S2F8C2	27	16	45	12	528.8	529.7	531.4	533.5
LF	8	25	47	20	522.6	525.7	529.3	531.7

LUMO, which explains the enhanced reduction ability observed upon substitution of Co for Fe in TPR. In addition, if it is easier for electrons to transfer from the valence band to the conduction band, lower photon energy is needed to excite the electros under UV radiation. Indeed, this is the case in the UV-Vis spectroscopic study of L8S2F and L8S2C (see Figure 6b).

The results in Figure 4 give evidence in support of the conclusions from TPR and TPSR, describing that there are two different periods or mechanisms for oxygen removal explained by the change in the oxidation state of the B-site cation. During the first period, Fe^{4+} is reduced to Fe^{3+} and the reducible oxygen gives rise to the total combustion of methane to form CO_2 and water. In the course of the second period, Fe^{3+} is reduced to Fe^{2+} resulting in the release of oxygen from the bulk of the material, resulting in the partial oxidation of methane. Moreover, in the first step, the surface oxygen is considered what gives the total methane combustion, while in the second step, the lattice oxygen diffuses to the surface and reacts with methane to give the selective oxidation products such as CO and H_2. The fact that the amount of CO_2 and water produced increases with the Sr^{2+} content in the perovskites confirms the increased amount of surface oxygen as a result of the substitution of Sr^{2+} for La^{3+}. The formation of oxygen vacancies results in more rapid transport of oxygen from the bulk to the surface and therefore less selective oxidation products.

3.7 Origin of composition-dependent reaction kinetics

To unravel the origin of the different CO selectivity of the different perovskite catalysts, we further studied the oxygen mobility in bulk perovskite by performing DFT calculations. It is acknowledged that formation of vacancies is essential to oxygen bulk diffusion, which is accompanied by electron transfer from oxygen to the remaining defective structure and can be described as

$$2B_B^X + O_O^\delta \rightarrow \left\{B_B^{'} - V_O^{\bullet\bullet} - B_B^{'}\right\} + \frac{1}{2}O_2(g) \quad (5)$$

where B_B^X and $B_B^{'}$ represent the transition metal before oxygen atom is removed and after oxygen vacancy is formed, respectively, and O_O^δ and $V_O^{\bullet\bullet}$ denote the oxygen ion bridging the two transition metals and the resultant oxygen vacancy, respectively[62]. Thus, the oxygen vacancy formation energy ($\Delta E_{f,vac}$) can be calculated as

$$\Delta E_{f,vac} = E_{defective} + \frac{1}{2}E_{O_2} - E_{perfect} \quad (6)$$

where $E_{perfect}$ and $E_{defective}$ are the total energies of the stoichiometric perovskite structure and its fully relaxed supercell with an oxygen atom removed from the lattice, respectively, and E_{O_2} is the total energy of a free oxygen molecule in its triplet state and has been corrected by fitting the formation energetics of nontransition-metal oxides to available experimental data[39]. Unlike the pseudocubic $LaFeO_3$ containing only two different types of oxygen ions[53], the substituted perovskites adopt a lowered symmetry with the introduction of Sr and Co into the A and B sites and thus have more inequivalent oxygen/vacancy sites. As for L5S5F and L5S5C, there are 4 different oxygen sites while L8S2F and L5S5F5C5 have 8 and 6 different oxygen sites, respectively. The calculated oxygen vacancy formation energies are summarized in Table S2. Unless otherwise specified, only the lowest oxygen vacancy formation energy is reported for each material in this work.

From Figure 8a, one can see that the oxygen vacancy formation energy decreases with the increasing the Sr^{2+} and Co^{3+} contents, implying that both substitution of La^{3+} for Sr^{2+} and Fe^{3+} for Co^{3+} make the perovskites more reducible; that is, the oxygen vacancy would be more readily formed. The reason that increasing the Sr^{2+} and Co^{3+} contents may lower the oxygen vacancy formation energy lies in the correlation established between the $\Delta E_{f,vac}$ and $|q_O|$, where $|q_O|$ denotes the calculated effective Bader charge on the oxygen ion in the perovskites. By decomposing the $\Delta E_{f,vac}$ into geometrical and electronic contributions, Zheng et al.[53] found that the variation of $\Delta E_{f,vac}$ is determined largely by the change in the bonding energy and the electrostatic interaction that is intimately related to the actual partial charges on the ions involved dominates the bonding in perovskites. Here the $\Delta E_{f,vac}$ is decomposed in the same way on $La_{1-x}Sr_xFeO_{3-\delta}$ (x = 0 and 0.2) and $La_{0.5}Sr_{0.5}Fe_{1-x}Co_xO_{3-\delta}$ (x = 0, 0.5, and 1). In particular, four oxygen atoms are successively removed from the LF perovskite to form vacancies, where the procedure proposed in a pervious study is used to ensure the most stable configuration at a specific oxygen deficiency is obtained[63]. It can be seen that plotting $\Delta E_{f,vac}$ against $|q_O|$ yields a straight line. The less negative the actual partial

charge on the oxygen ion, the weaker is the interaction between the oxygen and transition-metal ions, which causes the oxygen vacancy to be more readily formed.

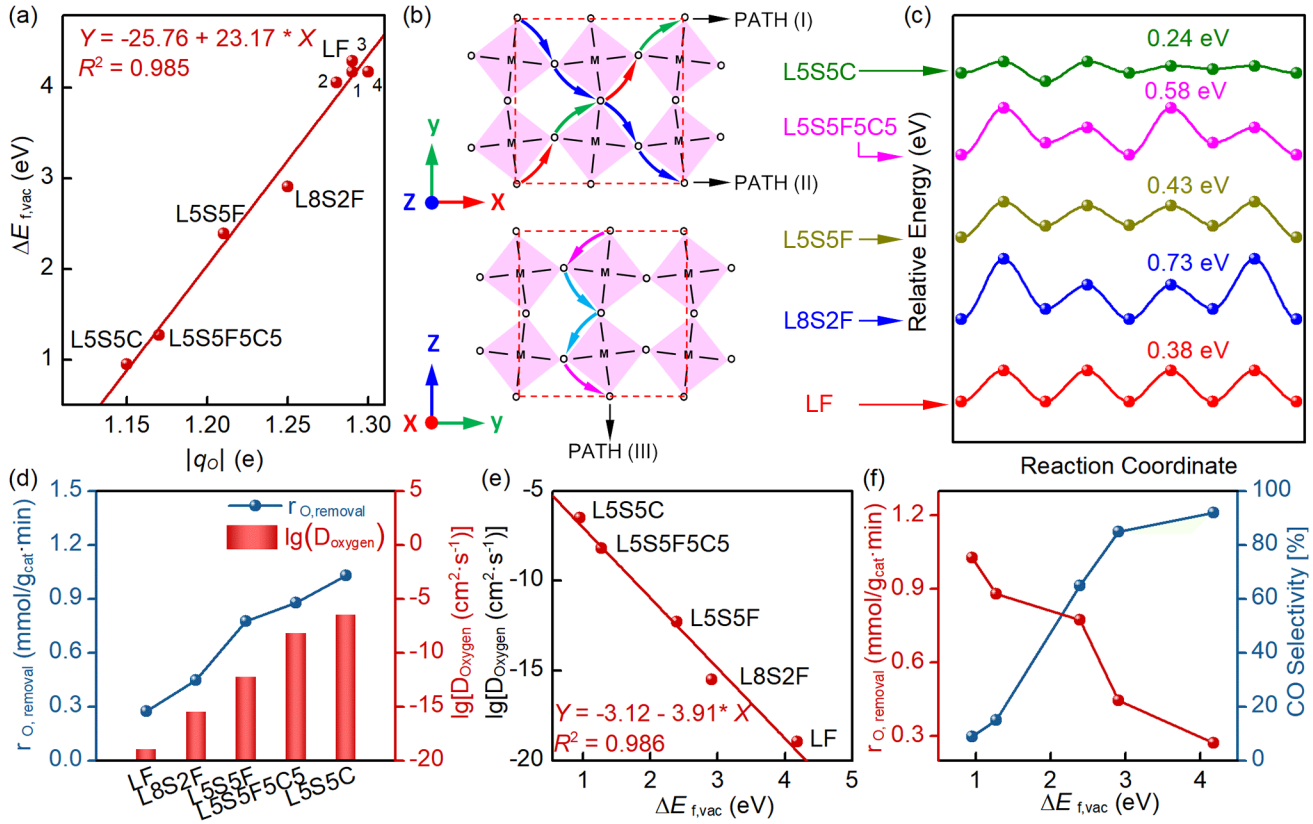

Figure 8. (a) Linear scaling relation between $\Delta E_{f,vac}$ and the actual partial charge on the oxygen ion (q_O), (b) illustration of three oxygen transport pathways, (c) calculated MEPs in the pseudocubic LF, L8S2F, L5S5F, L5S5FC5, and L5S5C, (d) relationship between the rate of O removal and the logarithm of D_{oxygen}, (e) dependence of the logarithm of D_{oxygen} on $\Delta E_{f,vac}$, and (f) plots of the rate of O removal and CO selectivity against $\Delta E_{f,vac}$.

It has been recognized that the oxygen migration in bulk perovskite occurs by the vacancy-mediated diffusion mechanism[53], in which the transport is due to discrete hops of oxygen ions between vacancies, and the oxygen diffusion coefficient can be calculated as

$$D_{oxygen} = \frac{C_{vac}}{3 - C_{vac}} D_{vac} \tag{7}$$

where C_{vac} and D_{vac} are the concentration of vacancies and the vacancy diffusion coefficient, respectively[64]. The details of the derivation of Eqs. 7 and 8 can be found in Sec. S3 in the Supporting Information. If we assume to a first approximation that equilibrium is established where the rate at which O_2 molecules are incorporated into the oxygen-deficient perovskite equals the rate at which O atoms recombine to escape from the solid, then C_{vac} can be obtained from[65]

$$K = exp\left(-\frac{\Delta G_{f,vac}}{RT}\right) = \frac{C_{vac} P_{O_2}^{1/2}}{(1-2C_{vac})^2 (3 - C_{vac})} \tag{8}$$

where K and $\Delta G_{f,vac}$ are the equilibrium constant and Gibbs free energy change for vacancy formation, respectively, and P_{O_2} is the partial pressure of O_2 in the gas phase[65]. Here the oxygen vacancy concentration is calculated at 900 °C and an O_2 partial pressure of 1 atm. As for the D_{vac}, the harmonic approximation to the transition state theory gives

$$D_{vac} = \frac{1}{6} d^2 \frac{\prod_i^{3N} \nu_i^{initial}}{\prod_i^{3N-1} \nu_i^{saddle}} exp\left(-\frac{\Delta G_{mig}}{RT}\right) \tag{9}$$

where d is the distance over which the hop occurs, ν_i is the vibrational frequencies of normal nodes, and ΔG_{mig} is the Gibbs free energy of activation for vacancy migration and can be calculated by first finding an minimum energy path and then making thermodynamic corrections. Our calculated results indicate that oxygen ions migrate preferentially along the diagonal of the *xy*-plane in LF and L5S5F5C5, and the only difference is that PATH(I) is kinetically favored in L5S5F5C5 while in LF PATH(II) that comprises only one repeating elementary step is preferred (see Figure 8b). By comparison, in L8S2F, L5S5F, and L5S5C, PATH(III) that is perpendicular to the *y* axis in the *yz*-plane is most favorable. The minimum energy paths (MEPs) for oxygen ion migration between energetically favorable

oxygen vacancies, together with the calculated energy barriers in all the five perovskites, are presented in Figure 8c and Table S4.

In Figure 8d, the experimentally determined rate of oxygen removal and the logarithm of the calculated diffusivity are correlated to the perovskites, and these two quantities are found to follow the same trend. Furthermore, a linear scaling relation can be established between the logarithm of the D_{oxygen} and $\Delta E_{f,vac}$ (see Figure 8e), indicating that $\Delta E_{f,vac}$ plays a major role in determining how rapidly oxygen can be transported in bulk perovskite, and hence how rapidly the redox reaction can occur. The underlying reason is that the $\Delta G_{f,vac}$ dominates the ΔG_{mig}, and a less positive $\Delta E_{f,vac}$ is indicative of more oxygen ions available to be removed and results in faster oxygen transport.

The last and most important information given by Figure 8 is that in part of the CO selectivity and the rate of oxygen removal change in opposite directions as $\Delta E_{f,vac}$ is increased. It is clear that weaker transition metal-oxygen bonding gives rise to a higher rate of oxygen consumption but would facilitate formation of CO_2 and H_2O more dramatically, and a high selectivity toward CO can only be attained at the expense of catalytic activity. To provide a rational interpretation of this connection, DFT calculations have been performed to examine the mechanism of partial oxidation of methane over the LF perovskite. The geometries of several key transition states and intermediates involved in the reaction network are shown in Figure 9. One can see that the reaction proceeds through CH_4 dissociation, followed by the oxidation of carbon-containing species by lattice

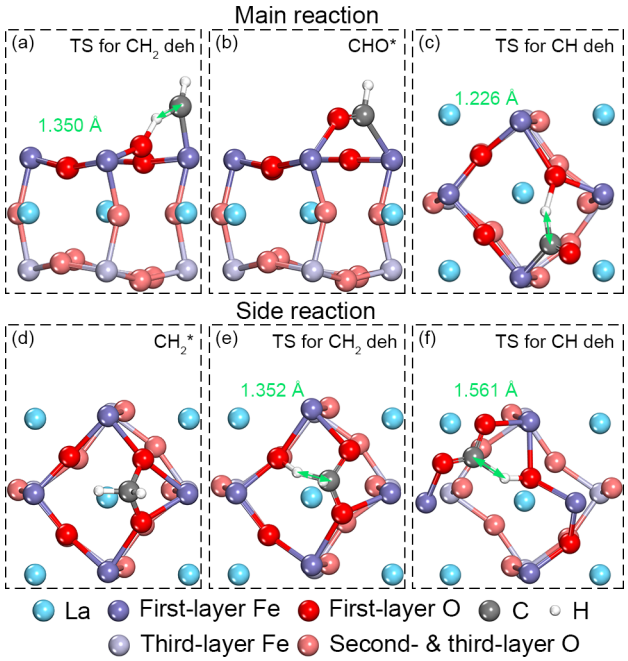

Figure 9. Geometries of (a) the transition state for CH_2 dehydrogenation, (b) adsorbed CHO, and (c) the transition state for CH dehydrogenation in the main reaction; geometries of (d) adsorbed CH_2, the transition states for (e) CH_2 and (f) CH dehydrogenation in the side reaction.

oxygen. The DFT results illustrate two different adsorption modes of CH_2 on the LF surface, as shown in Figure 9a and 9d, where CH_2 is adsorbed on one O and one Fe atom and on two adjunct O atoms, respectively. The different adsorption behaviors lead to two different reaction pathways. In the partial oxidation pathway (Figure 9 a-c), upon CH_2 dehydrogenation, CHO is formed above an oxygen vacancy and is further dehydrogenated to yield CO. The transition state for CH* dehydrogenation shown in Figure 9c requires two adjunct lattice oxygen ions. By comparison, the transition state for the elementary reaction step which leads to CO_2 formation (Figure 9 d-f) requires three adjunct lattice oxygen atoms. In the initial state for the total oxidation pathway, instead of interacting with surface Fe cations, CH_2 forms a σ bond to each of the two neighboring surface oxygen ions and sits somewhere between them (Figure 9d). In the subsequent CHO_2 dehydrogenation to produce CO_2, the C-H bond is broken in much the same way (Figure 9f), and a third oxygen ion participates in the reaction by attacking one of the C-H bonds. The ensemble sizes of the surface lattice oxygen are clearly different: 2 for the partial oxidation and 3 for the total oxidation of methane.

In light of this fact, the rate of formation of CO (r_{CO}) and CO_2 (r_{CO_2}) can be expressed as (see more details in Sec. S5 in the Supporting Information)

$$r_{CO} = k_{CO} P_{CH_4} [O_s]^2 \quad (10)$$

$$r_{CO_2} = k_{CO_2} P_{CH_4} [O_s]^3 \quad (11)$$

where k_{CO} and k_{CO_2} are the rate constant for the partial oxidation and total combustion of methane, respectively, P_{CH_4} represents the partial pressure of CH_4, and $[O_s]$ represents the surface oxygen concentration. The ratio of the rate of formation of CO_2 to CO depends not only on the surface oxygen concentration $[O_s]$ but also on the ratio of the rate constants k_{CO_2} / k_{CO}. For each perovskite, the rate constants k_{CO_2} and k_{CO} are fixed, but the selectivity changes remarkably with the oxygen content in the materials. It suggests that the surface oxygen concentration is the dominating factor influencing the selectivity. The higher $[O_s]$ is expected to result in a higher selectivity toward CO_2.

The rate of consumption of lattice oxygen can be written as

$$r_O = k_{CO} P_{CH_4} [O_s]^2 + 4 k_{CO_2} P_{CH_4} [O_s]^3 \quad (12)$$

If we assume by applying the pseudo steady state approximation that, during the major part of the reaction,

the rate of change of the concentration of surface oxygen is negligibly small:

$$\frac{d[O_s]}{dt} \approx 0 \tag{13}$$

then we may invoke Fick's first law of diffusion and write

$$k_{CO}P_{CH_4}[O_s]^2 + 4k_{CO_2}P_{CH_4}[O_s]^3 = \frac{D}{L}([O_b]-[O_s]) \tag{14}$$

where $[O_b]$ is the concentration in the lattice oxygen in the bulk, D is the diffusivity of lattice oxygen and L is the size of the perovskite crystal. Given the fact that the LF and L5S5C perovskites have a CO selectivity of 92% and 9%, Eq. 14 can be simplified as

$$k_{CO}P_{CH_4}[O_s]^2 = \frac{D}{L}([O_b]-[O_s]) \tag{15}$$

and

$$4k_{CO_2}P_{CH_4}[O_s]^3 = \frac{D}{L}([O_b]-[O_s]) \tag{16}$$

for the cases in which CO and CO2 formation dominate, respectively. Minor arrangement of Eq. (15) and (16) gives

$$\frac{[O_b]-[O_s]}{[O_s]^2} = \frac{Lk_{CO}P_{CH_4}}{D} = \Phi \tag{17}$$

and

$$\frac{[O_b]-[O_s]}{[O_s]^3} = \frac{4Lk_{CO_2}P_{CH_4}}{D} = \Phi' \tag{18}$$

where Φ and Φ' provide a measure of the relative ratio of the surface reactions rate to the diffusion rate of the lattice oxygen. It can be used to gauge how strongly the reaction rate is affected by the bulk diffusion of the lattice oxygen. The larger Φ and Φ' values presents a stronger diffusion limitation. The relationship among $[O_s]$, $[O_b]$, and Φ is plotted in Figure 10, in which the $[O_b]$ lies between 12.36 mmol/g_{cat} and 10.65 mmol/g_{cat}, corresponding to the oxygen deficiency of 0 and 0.05, respectively. Both experimental[26] and theoretical[63] studies have demonstrated that the maximum possible oxygen deficiency in LF is 0.05, upon which phase transition and separation would take place. From the figure, one can see that, regardless of the partial oxidation or total oxidation dominating, the lower the values of Φ and Φ', the higher is the surface oxygen concentration at a given $[O_b]$.

Thus, LF and L8S2F have relatively lower oxygen mobility and are expected to have a larger Φ and Φ' values and a lower $[O_s]$, and thus prefers the partial oxidation of methane. The $La_{0.5}Sr_{0.5}Fe_{1-x}Co_xO_{3-\delta}$ (x = 0, 0.5, and 1) perovskites with higher oxygen mobility provide

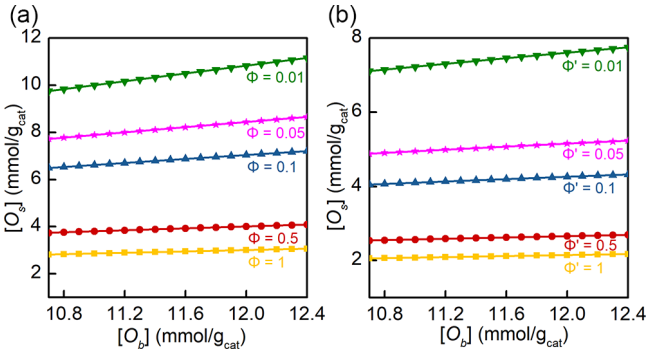

Figure 10. Relationship among $[O_s]$, $[O_b]$, and Φ at (a) partial oxidation and (b) total oxidation dominating.

high rate of diffusion, and higher $[O_s]$, and thus are well suited to the total oxidation of methane. As proposed by Tu et al.[66], the surface density of oxygen $[O_s]/[*]$ which is defined as the oxygen-to-unoccupied metal site ratio is proportional to P_{CO_2}/P_{CO}. Therefore, a higher surface oxygen concentration is expected to be at a higher P_{CO_2}/P_{CO} ratio. Experimentally, the higher pressure of CO_2 than CO is observed, suggesting a higher surface oxygen concentration density on $La_{0.5}Sr_{0.5}Fe_{1-x}Co_xO_{3-\delta}$ (x = 0, 0.5) than on the LF and L8S2F perovskites. Consequently, a lower CO selectivity and higher selectivity toward CO_2 are expected on $La_{0.5}Sr_{0.5}Fe_{1-x}Co_xO_{3-\delta}$ (x = 0, 0.5) than on the LF and L8S2F perovskites, which agrees well with the experimental observation.

In addition, Figure 10 also illustrates the dependence of the surface oxygen concentration on the bulk oxygen concentration. On the fresh catalysts, the high bulk oxygen concentration results in a high surface oxygen concentration, and hence high selectivity toward CO_2. When oxygen atoms are gradually removed, the reduced bulk oxygen concentration $[O_b]$ results in a slightly lower surface oxygen concentration, causing the catalyst to be more selective for synthesis gas production, which is again consistent well with the experimental observation.

4. Conclusion

We report here a strong dependence of the activity and selectivity of chemical looping methane oxidation on the oxygen mobility in the $La_{1-x}Sr_xFeO_{3-\delta}$ (x = 0, 0.2, and 0.5) and $La_{0.5}Sr_{0.5}Fe_{1-x}Co_xO_{3-\delta}$ (x = 0 and 0.5) perovskites by carrying out a combined experimental and DFT study. The oxygen mobility determines the surface oxygen concentration or the oxygen vacancy concentration on perovskites during the reaction, which depends strongly on the bulk oxygen concentration and the relative rate of the lattice oxygen diffusion with respect to the surface reaction. A lower surface oxygen concentration is beneficial to a lower selectivity to CO_2, while a higher surface oxygen concentration is beneficial to the activity. There is thus an optimal surface oxygen concentration for the selective methane oxidation. The oxygen mobility described by the formation energy of oxygen vacancy is

found to be the key parameter to tune the surface oxygen concentration. The formation energy of oxygen vacancy can be used as a descriptor of the selectivity of methane oxidation.

More importantly, we provide a guideline for the rational design of perovskite materials for the selective oxidation. By manipulating oxygen mobility of the perovskites, methane oxidation can change from selective oxidation to synthesis gas to fully total combustion. For the $LaFeO_3$ perovskite, substitution of Co^{3+} for Fe^{3+} at the B site and substitution of Sr^{2+} for La^{2+} at the A site would reduce the formation energy of oxygen vacancy and increase the oxygen mobility. $LaFeO_3$ and $La_{0.8}Sr_{0.2}FeO_3$ perovskites with relatively low oxygen mobility are promising selective catalysts for the partial oxidation process, whereas the $La_{0.5}Sr_{0.5}Fe_{1-x}Co_xO_{3-\delta}$ (x = 0, 0.5, 1) perovskites with relatively high oxygen mobility are well suited to methane total combustion. Moreover, the insight gained here is expected to greatly improve our understanding of selective oxidation reactions on oxides in general and design more selective catalysts.

ASSOCIATED CONTENT

Supporting Information: CH_4 conversion and CO selectivity as a function of temperature for LF and L8S2F, molar flows of CH_4, H_2, CO, CO_2, and H_2O and CH_4 conversion, CO selectivity and H_2/CO ratio of partial oxidation of methane during five oxidation-reduction cycles over L8S2F perovskite, MS signals from re-oxidation after five cyclic experiments and from re-oxidation of LF, calculated oxygen vacancy formation energies and energy barriers for the kinetically most favorable oxygen diffusion pathways in the pseudocubic LF, L8S2F, L5S5F, L5S5F5C5, and L5S5C perovskites.

AUTHOR INFORMATION

Corresponding Author

* Email: yanzhu@ecust.edu.cn (Yi-An Zhu)
de.chen@ntnu.no (De Chen)

Present Addresses

† Present address: Equinor, Mongstad, 5954, Monstad, Norway (Erlend Bjørgum)

‡ Present address: Volvo car cooperation, Gothenburg 41715, Sweden (Oana Mihai)

Notes

The authors declare no competing financial interest.

ACKNOWLEDGMENT

The financial support from the Norwegian Research Council through the KOSK program, the Norwegian University of Science and Technology (NTNU), and Natural Science Foundation of China (21473053, 91645122, and U1663221) is greatly acknowledged. The computational time is provided by the Notur project (NN4685k).

REFERENCES

1. Duprez, D.; Cavani, F., Handbook of Advanced Methods and Processes in Oxidation Catalysis: From Laboratory to Industry. 2014; p 1-1035.
2. Valange, S.; Védrine, J. C., General and Prospective Views on Oxidation Reactions in Heterogeneous Catalysis. Catalysts **2018,** 8 (10), 483.
3. Gao, F. Y.; Tang, X. L.; Yi, H. H.; Zhao, S. Z.; Li, C. L.; Li, J. Y.; Shi, Y. R.; Meng, X. M., A Review on Selective Catalytic Reduction of NO_x by NH_3 over Mn-Based Catalysts at Low Temperatures: Catalysts, Mechanisms, Kinetics and DFT Calculations. Catalysts **2017,** 7 (7), 199.
4. Costentin, C.; Robert, M.; Saveant, J. M., Catalysis of the Electrochemical Reduction of Carbon Dioxide. Chem. Soc. Rev. **2013,** 42 (6), 2423-2436.
5. Wang, Z. L.; Xu, D.; Xu, J. J.; Zhang, X. B., Oxygen Electrocatalysts in Metal-Air Batteries: from Aqueous to Nonaqueous Electrolytes. Chem. Soc. Rev. **2014,** 43 (22), 7746-7786.
6. McFarland, E. W.; Metiu, H., Catalysis by Doped Oxides. Chem. Rev. **2013,** 113 (6), 4391-4427.
7. Grasselli, R. K., Fundamental Principles of Selective Heterogeneous Oxidation Catalysis. Top. Catal. **2002,** 21 (1), 79-88.
8. Getsoian, A. B.; Zhai, Z.; Bell, A. T., Band-Gap Energy as a Descriptor of Catalytic Activity for Propene Oxidation over Mixed Metal Oxide Catalysts. J. Am. Chem. Soc. **2014,** 136 (39), 13684-13697.
9. Hwang, J.; Rao, R.; Giordano, L.; Katayama, Y.; Yu, Y.; Shao-Horn, Y., Perovskites in Catalysis and Electrocatalysis. Science **2017,** 358, 751-756.
10. Royer, S.; Duprez, D.; Can, F.; Courtois, X.; Batiot-Dupeyrat, C.; Laassiri, S.; Alamdari, H., Perovskites as Substitutes of Noble Metals for Heterogeneous Catalysis: Dream or Reality. Chem. Rev. **2014,** 114 (20), 10292-10368.
11. Zhu, H.; Zhang, P.; Dai, S., Recent Advances of Lanthanum-Based Perovskite Oxides for Catalysis. ACS Catal. **2015,** 5 (11), 6370-6385.
12. Kubicek, M.; Bork, A. H.; Rupp, J. L. M., Perovskite Oxides – A Review on a Versatile Material Class for Solar-to-Fuel Conversion Processes. J. Mater. Chem. A **2017,** 5 (24), 11983-12000.
13. Gao, Y.; Haeri, F.; He, F.; Li, F., Alkali Metal-Promoted $La_xSr_{2-x}FeO_{4-\delta}$ Redox Catalysts for Chemical Looping Oxidative Dehydrogenation of Ethane. ACS Catal. **2018,** 8 (3), 1757-1766.
14. Fathi, M.; Bjorgum, E.; Viig, T.; Rokstad, O. A., Partial Oxidation of Methane to Synthesis Gas: Elimination of Gas Phase Oxygen. Catal. Today **2000,** 63, 489-497.
15. Fathi, M.; Monnet, F.; Schuurman, Y.; Holmen, A.; Mirodatos, C., Reactive Oxygen Species on Platinum Gauzes during Partial Oxidation of Methane into Synthesis Gas. J. Catal. **2000,** 190, 439-445.
16. Kang, Y.; Tian, M.; Huang, C.; Lin, J.; Hou, B.; Pan, X.; Li, L.; Rykov, A. I.; Wang, J.; Wang, X., Improving Syngas Selectivity of Fe_2O_3/Al_2O_3 with Yttrium Modification in Chemical Looping Methane Conversion. ACS Catal. **2019,** 9 (9), 8373-8382.
17. Shen, Q.; Huang, F.; Tian, M.; Zhu, Y.; Li, L.; Wang, J.; Wang, X., Effect of Regeneration Period on the Selectivity of Synthesis Gas of Ba-Hexaaluminates in Chemical Looping Partial Oxidation of Methane. ACS Catal. **2019,** 9 (1), 722-731.
18. Zhu, X.; Li, K.; Neal, L.; Li, F., Perovskites as Geo-inspired Oxygen Storage Materials for Chemical Looping and Three-Way Catalysis: A Perspective. ACS Catal. **2018,** 8 (9), 8213-8236.
19. Başhan, V.; Ust, Y., Perovskite Catalysts for Methane Combustion: Applications, Design, Effects for Reactivity and Partial Oxidation. Int. J. Energy Res. **2019**. doi: 10.1002/er.4721.
20. Tang, M.; Xu, L.; Fan, M., Progress in Oxygen Carrier Development of Methane-Based Chemical-Looping Reforming: A Review. Appl. Energy **2015,** 151, 143-156.

21. Zeng, L.; Cheng, Z.; Fan, J. A.; Fan, L.-S.; Gong, J., Metal Oxide Redox Chemistry for Chemical Looping Processes. Nat. Rev. Chem. **2018,** 2 (11), 349-364.

22. Seiyama, T., Total Oxidation of Hydrocarbons on Perovskite Oxides. Catal. Rev.-Sci. Eng. **1992,** 34, 281-300.

23. Ciambelli, P.; Cimino, S.; Rossi, S.; Lisi, L.; Minelli, G.; Porta, P.; Russo, G., $AFeO_3$ (A = La, Nd, Sm) and $LaFe_{1-x}Mg_xO_3$ Perovskites as Methane Combustion and CO Oxidation Catalysts: Structural, Redox and Catalytic Properties. Appl. Catal. B-Environ. **2001,** 29, 239-250.

24. Ciambelli, P.; Cimino, S.; Lasorella, G.; Lisi, L.; Rossi, S.; Faticanti, M.; Minelli, G.; Porta, P., CO Oxidation and Methane Combustion on $LaAl_{1-x}Fe_xO_3$ Perovskite Solid Solutions. Appl. Catal. B-Environ. **2002,** 37, 231-241.

25. Zhang, H. M.; Shimizu, Y.; Teraoka, Y.; Miura, N.; Yamazoe, N., Oxygen Sorption and Catalytic Properties of $La_{1-x}Sr_xCo_{1-y}Fe_yO_3$ Perovskite-Type Oxides. J. Catal. **1990,** 121, 432-440.

26. Mihai, O.; Chen, D.; Holmen, A., Catalytic Consequence of Oxygen of Lanthanum Ferrite Perovskite in Chemical Looping Reforming of Methane. Ind. Eng. Chem. Res. **2011,** 50 (5), 2613-2621.

27. Mihai, O.; Chen, D.; Holmen, A., Chemical Looping Methane Partial Oxidation: The Effect of the Crystal Size and O Content of $LaFeO_3$. J. Catal. **2012,** 293, 175–185.

28. Cheng, X.; Fabbri, E.; Nachtegaal, M.; Castelli, I. E.; El Kazzi, M.; Haumont, R.; Marzari, N.; Schmidt, T. J., Oxygen Evolution Reaction on $La_{1-x}Sr_xCoO_3$ Perovskites: A Combined Experimental and Theoretical Study of Their Structural, Electronic, and Electrochemical Properties. Chem. Mater. **2015,** 27 (22), 7662-7672.

29. Hong, W. T.; Risch, M.; Stoerzinger, K. A.; Grimaud, A.; Suntivich, J.; Shao-Horn, Y., Toward the Rational Design of Non-Precious Transition Metal Oxides for Oxygen Electrocatalysis. Energy Environ. Sci. **2015,** 8 (5), 1404-1427.

30. Buelens, L.; Galvita, V.; Poelman, H.; Detavernier, C.; Marin, G., Super-Dry Reforming of Methane Intensifies CO_2 Utilization via Le Chatelier's Principle. Science **2016,** 354, 449-452.

31. Chick, L. A.; Pederson, L. R.; Maupin, G. D.; Bates, J. L.; Thomas, L. E.; Exarhos, G. J., Glycine-Nitrate Combustion Synthesis of Oxide Ceramic Powders. Mater. Lett. **1990,** 10 (1), 6-12.

32. Barton, D. G.; Shtein, M.; Wilson, R. D.; Soled, S. L.; Iglesia, E., Structure and Electronic Properties of Solid Acids Based on Tungsten Oxide Nanostructures. J. Phys. Chem. B **1999,** 103 (4), 630-640.

33. Kresse, G.; Furthmüller, J., Efficient Iterative Schemes for Ab Initio Total-Energy Calculations Using a Plane-Wave Basis Set. Phys. Rev. B **1996,** 54 (16), 11169-11186.

34. Kresse, G.; Hafner, J., Ab Initiomolecular Dynamics for Open-Shell Transition Metals. Phys. Rev. B **1993,** 48 (17), 13115-13118.

35. Blöchl, P. E., Projector Augmented-Wave Method. Phys. Rev. B **1994,** 50 (24), 17953-17979.

36. Wellendorff, J.; Lundgaard, K. T.; Møgelhøj, A.; Petzold, V.; Landis, D. D.; Nørskov, J. K.; Bligaard, T.; Jacobsen, K. W., Density Functionals for Surface Science: Exchange-Correlation Model Development with Bayesian Error Estimation. Phys. Rev. B **2012,** 85 (23), 235149.

37. Monkhorst, H. J.; Pack, J. D., Special Points for Brillouin-Zone Integrations. Phys. Rev. B **1976,** 13 (12), 5188-5192.

38. Cohen, A. J.; Mori-Sánchez, P.; Yang, W., Insights into Current Limitations of Density Functional Theory. Science **2008,** 321 (5890), 792-794.

39. Li, Y.; Zheng, Y.-S.; Zhu, Y.-A.; Sui, Z.-J.; Zhou, X.-G.; Chen, D.; Yuan, W.-K., BEEF-vdW+U Method Applied to Perovskites: Thermodynamic, Structural, Electronic, and Magnetic Properties. J. Phys.: Condens. Matter **2019,** 31 (14), 145901.

40. Glazer, M., Simple Ways of Determining Perovskite Structure. Acta Crystallogr. Sect. A **1975,** 31, 756-762.

41. Lufaso, M.; Woodward, P., Prediction of the Crystal Structures of Perovskites Using the Software Program SpuDS. Acta Crystallogr. Sect. B-Struct. Sci. **2002,** 58, C340-C340.

42. Murnaghan, F. D., The Compressibility of Media under Extreme Pressures. Proc. Natl. Acad. Sci. U.S.A. **1944,** 30 (9), 244-247.

43. Li, R.; Yu, C.; Shen, S., Partial Oxidation of Methane to Syngas Using Lattice Oxygen of $La_{1-x}Sr_xFeO_3$ Perovskite Oxide Catalysts Instead of Molecular Oxygen. J. Nat. Gas Chem. **2002,** 11, 137-144.

44. Tanaka, H.; Misono, M., Advances in Designing Perovskite Catalysts. Curr. Opin. Solid State Mater. Sci. **2001,** 5, 381-387.

45. Ciambelli, P.; Cimino, S.; Lisi, L.; Faticanti, M.; Minelli, G.; Pettiti, I.; Porta, P., La, Ca and Fe Oxide Perovskites: Preparation, Characterization and Catalytic Properties for Methane Combustion. Appl. Catal. B-Environ. **2001,** 33, 193-203.

46. Bhalla, A.; Guo, R.; Roy, R., Material Research Innovations. Mater. Res. Innov . **2000,** 4, 3-26.

47. Lein, H.; Wiik, K.; Grande, T., Thermal and Chemical Expansion of Mixed Conducting $La_{0.5}Sr_{0.5}Fe_{1-x}Co_xO_{3-\delta}$ Materials. Solid State Ion. **2006,** 177, 1795–1798.

48. Shannon, R., Revised Effective Ionic Radii and Systematic Studies of Interatomic Distances in Halides and Chalcogenides. Acta Crystallogr. Sect. A **1976,** 32, 751-767.

49. Cheng, J.; Navrotsky, A.; Zhou, X.-D.; Anderson, H. U., Thermochemistry of $La_{1-x}Sr_xFeO_{3-\delta}$ Solid Solutions ($0.0 \leqslant x \leqslant 1.0$, $0.0 \leqslant \delta \leqslant 0.5$). Chem. Mater. **2005,** 17 (8), 2197-2207.

50. Zwinkels, M.; Järås, S.; Menon, P.; Griffin, T., Catalytic Materials for High-Temperature Combustion. Catal. Rev. **1993,** 35, 319-358.

51. Nakamura, T.; Misono, M.; Yoneda, Y., Reduction-Oxidation and Catalytic Properties of Perovskite-Type Mixed Oxide Catalysts ($La_{1-x}Sr_xCoO_3$). Chem. Lett. **1981,** 10, 1589-1592.

52. Takeda, Y.; Kanno, R.; Takada, T.; Yamamoto, O.; Takano, M.; Bando, Y., Phase relation and oxygen-nonstoichiometry of Perovskite-like Compound $SrCoO_x$ ($2.29 < x > 2.80$). Z. Anorg. Allg. Chem. **1986,** 540, 259-270.

53. Zheng, Y.-S.; Zhang, M.; Li, Q.; Zhu, Y.-A.; Sui, Z.-J.; Chen, D.; Zhou, X.-G., Electronic Origin of Oxygen Transport Behavior in La-Based Perovskites: A Density Functional Theory Study. J. Phys. Chem. C **2019,** 123 (1), 275-290.

54. Spinicci, R.; Tofanari, A.; Delmastro, A.; Mazza, D.; Ronchetti, S., Catalytic Properties of Stoichiometric and Non-Stoichiometric $LaFeO_3$ Perovskite for Total Oxidation of Methane. Mater. Chem. Phys. **2002,** 76, 20-25.

55. Kharton, V. V.; Yaremchenko, A. A.; Valente, A. A.; Sobyanin, V. A.; Belyaev, V. D.; Semin, G. L.; Veniaminov, S. A.; Tsipis, E. V.; Shaula, A. L.; Frade, J. R.; Rocha, J., Methane Oxidation over Fe-, Co-, Ni- and V-Containing Mixed Conductors. Solid State Ion. **2005,** 176 (7-8), 781-791.

56. Macht, J.; Iglesia, E., Structure and Function of Oxide Nanostructures: Catalytic Consequences of Size and Composition. Phys. Chem. Chem. Phys. **2008,** 10, 5331-5343.

57. Poulin, S.; França, R.; Moreau-Bélanger, L.; Sacher, E., Confirmation of X-ray Photoelectron Spectroscopy Peak Attributions of Nanoparticulate Iron Oxides, Using Symmetric Peak Component Line Shapes. J. Phys. Chem. C **2010,** 114 (24), 10711-10718.

58. Zhao, X.; Yang, Q.; Cui, J., XPS Study of Surface Absorbed Oxygen of ABO_3 Mixed Oxides. J. Rare Earths **2008,** 26 (4), 511-514.

59. Mickevicius, S.; Grebinskij, S.; Bondarenka, V.; Vengalis, B.; Šliužienė, K.; Orlowski, B. A.; Osinniy, V.; Drube, W., Investigation of Epitaxial $LaNiO_{3-x}$ Thin Films by High-Energy XPS. J. Alloys Compd. **2006,** 423, 107-111.

60. Asha, A.; Critchley, J.; Nix, R., Molecular Adsorption Characteristics of Lanthanum Oxide Surfaces: The Interaction of Water with Oxide Overlayers Grown on Cu(111). Surf. Sci. **1998,** 405, 201-214.

61. Dupin, J.-C.; Gonbeau, D.; Vinatier, P.; Levasseur, A., Systematic XPS Studies of Metal Oxides, Hydroxides and Peroxides. Phys. Chem. Chem. Phys. **2000,** 2 (6), 1319-1324.

62. Kröger, F.; Vink, H., Relations between the Concentrations of Imperfections in Crystalline Solids. Solid State Phys. **1956,** 3, 307-435.

63. Li, Q.; Deng, Y.-X.; Zhu, Y.-A.; Li, Y.; Sui, Z.-J.; Chen, D.; Yuan, W.-K., Structural stability of Lanthanum-based oxygen-deficient perovskites in redox catalysis: A density functional theory study. Catal. Today **2018**. doi: 10.1016/j.cattod.2018.04.070.

64. Ishigaki, T.; Yamauchi, S.; Kishio, K.; Mizusaki, J.; Fueki, K., Diffusion of Oxide Ion Vacancies in Perovskite-Type Oxides. J. Solid State Chem. **1988,** 73 (1), 179-187.

65. Holt, A.; Norby, T.; Glenne, R., Defects and Transport in $SrFe_{1-x}Co_xO_{3-\delta}$. Ionics **1999,** 5 (5), 434-443.

66. Tu, W.; Ghoussoub, M.; Singh, C. V.; Chin, Y.-H. C., Consequences of Surface Oxophilicity of Ni, Ni-Co, and Co Clusters on Methane Activation. J. Am. Chem. Soc. **2017,** 139 (20), 6928-6945.

TOC Graphic